

Physical Principles and Technology of Clinical PET Imaging[†]

DW Townsend,¹PhD

Abstract

Molecular imaging with positron-emitting radionuclides is playing an increasingly important role in the diagnosis and staging of malignant disease and in monitoring response to therapy. To meet this challenge, significant improvements in the performance of the imaging technology have been achieved in recent years. Such developments are subject to the constraints imposed by the physics of positron emission tomography (PET) and the main objectives in designing or improving PET scanners are to achieve high spatial resolution and sensitivity while maximising the true coincidence count rate relative to contributions from noise processes. Noise contributions in PET include not only statistical effects associated with photon counting but also background processes such as scatter and random coincidences. The recent developments of new, faster scintillators and electronics for PET detectors, as well as statistically-based algorithms that reconstruct fully three-dimensional (3D) PET images in minutes, have dramatically reduced clinical imaging times while improving image quality. A recent advance, the combination of functional imaging and computed tomography (CT) in the PET/CT scanner has further reduced the study duration by eliminating the lengthy PET transmission scan and providing accurate anatomical localisation of functional abnormalities. PET imaging technology has now improved to where a combined anatomical and functional clinical study can be completed in less than 10 minutes – although taking advantage of such high throughput potential will challenge patient management in diagnostic imaging departments. This paper reviews the physical principles underlying PET and summarises the recent developments in PET scanner technology, from the introduction of new PET detectors to the development of the combined PET/CT scanner.

Ann Acad Med Singapore 2004;33:133-45

Key words: Computed, Emission, Imaging, Instrumentation, Three-dimensional, Tomography

Introduction

The past few years have seen the transition of positron emission tomography (PET) from the research domain into mainstream clinical applications for oncology.¹ The emergence of PET as the functional imaging modality of choice for diagnosis, staging, therapy monitoring and assessment of recurrence in cancer has led to an increasing demand for this advanced imaging technology. The recognition that functional imaging modalities such as PET may provide an earlier diagnosis and more accurate staging than conventional anatomical imaging has promoted the technology, particularly as PET is now a reimbursed procedure in the US for many types of cancer. Although

PET offers an extensive array of different radio-pharmaceuticals, or molecular probes, to image different aspects of physiology and tumour biology, currently the most widely used PET tracer is the fluorinated analogue of glucose, FDG. The increased uptake of glucose in malignant cells has been well known for many years² and while FDG is not a specific probe for cancer, non-specificity can be a useful property when identifying and staging disease by a survey of the whole body. The widespread use of FDG is facilitated by the half-life of ¹⁸F (110 minutes) that is convenient for transportation from a remote cyclotron and compatible with typical whole-body PET imaging times of ≥ 30 minutes.

¹ Professor, Departments of Medicine and Radiology
University of Tennessee Medical Center, Tennessee, USA

Address for Reprints: Dr David W Townsend, Department of Medicine, University of Tennessee Medical Center, 1924 Alcoa Highway, Knoxville, Tennessee 37920-6999, USA

Email: dtownsend@mc.utmck.edu

[†] David W Townsend, PhD, is a Senior Consultant for CPS Innovations, Knoxville, TN, USA. He is financially compensated for his consultancy work with CPS Innovations. CPS Innovations is the manufacturer of one of the PET/CT scanners described in this manuscript. This design of PET/CT is marketed commercially by Siemens Medical Solutions and CTI Molecular Imaging. Dr Townsend designed and built the first combined PET/CT scanner in collaboration with Dr Ron Nutt who was then President of CPS Innovations.

Based on an estimate of the number of cancer patients in the US who could potentially benefit from a reimbursable whole-body FDG-PET scan, the demand should far exceed the currently available capacity of PET scanners. That, and the potential for an eventual reduction in the present levels of reimbursement, has put pressure on the developers of PET imaging equipment to reduce the lengthy scan times traditionally associated with functional imaging and thereby increase daily patient throughput. Fortunately, a number of recent developments in detector technology and image reconstruction methodology have successfully resulted in reducing PET imaging times to ≤ 10 minutes, for certain patients. Another contributing factor to this reduction in scan duration has been the incorporation of anatomical imaging by computed tomography (CT) in the combined PET/CT scanner. The combination of PET and CT not only eliminates the requirement to perform a lengthy PET transmission scan, but also provides accurately registered anatomical and functional images. While the uptake of FDG in all cells using glucose yields some low-resolution anatomical information from the PET scan alone, the combined PET/CT scanner offers high-resolution anatomical imaging irrespective of the specificity of the PET probe. Imaging anatomy and function will be essential as increasingly specific PET probes are developed for clinical use.

This paper summarises the physical principles of positron tomography and their impact on the design and

performance of PET scanners. Detector technology is discussed, including the transition to a new scintillator material that significantly improves scanner performance and is particularly suited to three-dimensional (3D) acquisition. The rationale for the transition from PET to combined PET/CT will be given and some current PET/CT scanner designs reviewed. The steps in a typical PET/CT protocol will be discussed and since they include the use of CT-based attenuation correction factors (ACFs) obtained by scaling the CT images to the PET photon energy, an appropriate scaling algorithm will be described.

Physical Principles of PET Imaging

The principles of imaging tissue function *in vivo* with PET are summarised in Figure 1. Multiple steps are involved in the PET process, beginning with the selection and production of a suitable molecular probe, a pharmaceutical labelled with a positron-emitting radionuclide, the administration of the probe to the patient and finally the imaging of the distribution of the probe in the patient. Positron emitters are neutron-deficient isotopes that achieve stability through the nuclear transmutation of a proton into a neutron. As shown in Figure 1a, this process involves the emission of a positive electron, or positron (e^+) and an electron neutrino (ν_e). The energy spectrum of the emitted positron depends on the specific isotope, with typical endpoint energies varying from 0.6 MeV for ^{18}F up to 3.4 MeV for ^{82}Rb . After emission, the positron loses energy

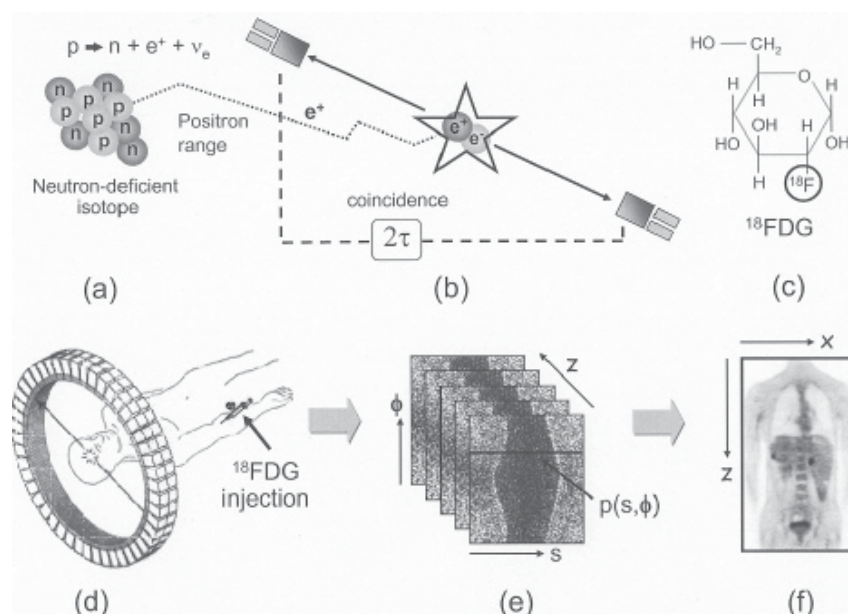


Fig. 1. The principles of PET imaging shown schematically, including: (a) the decay of a neutron-deficient, positron-emitting isotope, (b) the detection in coincidence of the annihilation photons within a time window of 2τ ns, (c) the glucose analogue deoxyglucose labelled with the positron-emitter ^{18}F to form the radiopharmaceutical FDG, (d) the injection of the labelled pharmaceutical and the detection of a pair of annihilation photons in coincidence by a multi-ring PET camera, (e) the collection of the positron annihilation events into sinograms where each element of the sinogram contains the number of annihilations in a specific projection direction, and (e) a coronal section of the final, reconstructed whole-body image mapping the utilisation of glucose throughout the patient.

through interactions with the surrounding tissue until it annihilates with an electron, as shown schematically in Figure 1b. The range the positron travels in tissue obviously depends on the energy with which it is emitted, and that, in turn, depends on the particular isotope. The 2 annihilation gamma rays are emitted in opposite directions and are detected in coincidence; in this example, a coincidence is defined by 2 photons that are registered within a time window of 2τ ns.

Positron emitters such as ^{18}F are used to label substrates like deoxyglucose (Fig. 1c) to create a radiopharmaceutical, FDG. The radioactive tag is then transported to the organ of interest by the circulation and through metabolism of the pharmaceutical it is incorporated into the organ. For FDG, the metabolic process is that of glucose utilisation. The radiopharmaceutical is injected into the patient who is then positioned in the PET scanner, a circular configuration of detectors, as shown in Figure 1d. The gamma ray pairs from positron annihilation are captured in coincidence by opposing detectors. The pairs of coincident photons, or events, detected are stored in matrices or sinograms where each row in the matrix represents a parallel projection $p(s, \phi)$ of the activity distribution in the patient at a specific angle (ϕ) and axial position (z), as shown in Figure 1e. An image reconstruction algorithm is applied to the sinograms to recover the underlying radioactivity distribution, thus indirectly mapping the functional process that created the distribution of positron emitter. For the radiopharmaceutical FDG, the results, as shown in Figure 1f, are images of FDG accumulation throughout the body that are closely related to tissue glucose utilisation.

The basis of PET is, therefore, that the pharmaceutical or substrate interacts with the body through a metabolic process; the radionuclide allows that interaction to be followed, mapped and measured. For medical applications of PET, the most important radionuclides, with half-lives in parentheses, are ^{15}O (2.03 minutes), ^{13}N (9.96 minutes), ^{11}C (20.4 minutes) and ^{18}F (109.8 minutes). For clinical applications, only ^{18}F is currently of importance in oncology due to the widespread use of FDG, and potentially ^{18}F for bone scanning. The maximum energy of the positron from the decay of ^{18}F is 0.633 MeV, with a mean range of 0.6 mm. It is, therefore, a nuclide with favourable properties for high-resolution PET imaging.

Spatial Resolution

The physics of positron emission imposes certain limitations on the spatial, temporal and contrast resolution that can be attained in a particular imaging situation. Positron range is obviously one limitation on the spatial resolution, since the goal is to map the distribution of positron emitters and not the distribution of annihilation

points. The energy carried by the positron may not be entirely dissipated during its journey in tissue and the annihilating electron-positron system could have a residual momentum. To conserve momentum, the annihilation photons are emitted less than 180 degrees apart, further contributing to a loss of spatial resolution because the 2 photons are assumed to be collinear and to form a straight line containing the point of emission of the positron. Neither of these assumptions is exact, and both positron range and acollinearity of the photons degrade spatial resolution. The contribution from acollinearity increases with increased separation of the detectors in coincidence, and is a maximum at the centre of the transverse field of view. For typical PET scanner designs, the contribution from photon acollinearity will be about 1.5 mm full-width at half-maximum (fwhm) for ^{18}F . While these physical effects place a lower limit on the spatial resolution that can be achieved with PET, contributions from the size and design of the PET detectors degrade the spatial resolution even more significantly in clinical PET scanners. Physical effects contribute 2 mm or less, whereas the spatial resolution of a PET scanner in a clinical imaging situation is, at best, 6 to 8 mm.

Scatter and Randoms

As with any imaging technique, not all acquired events contribute to the signal. Contributions to the background noise include photons that scatter prior to detection and photons from 2 unrelated annihilations that are erroneously assigned to a single positron emission, as shown schematically in Figure 2. For scattered events (Fig. 2a), one or both photons interact with the tissue before reaching

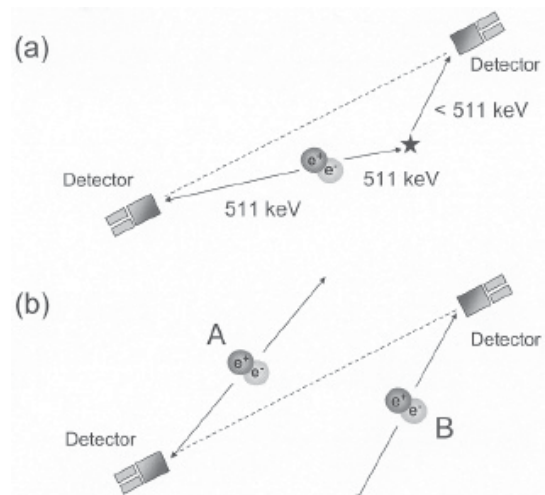


Fig. 2. Contributions to PET data acquired in addition to the true coincidences, where: (a) one (or both) photons scatter and lose energy before they reach the PET detectors and (b) two annihilation photons from different positron decays A and B are detected within the coincidence time window appearing to form a true coincidence; such events are called random coincidences.

the detectors and as a consequence the event is assigned incorrectly to the line joining the two detectors. The level of scatter, which is primarily due to the Compton process at this energy, is characterised by the scatter fraction (SF), the ratio of scattered events to total events. Random coincidences (Fig. 2b) are a consequence of 2 unrelated annihilation photons arriving within the time window used to define a coincidence. The random coincidence rate increases linearly with the width of the time window and quadratically with the rate of single photons interacting in the detectors. Both of these background processes introduce a bias into the reconstructed images, a bias that can be reduced or eliminated by modelling each process, although at the expense of increasing image noise.

Scattered photons could be identified and rejected by applying a simple energy threshold. However, as will be discussed in the section on “Imaging Technology for PET”, the energy resolution of current PET detectors is unable to accurately distinguish scattered from non-scattered photons above a certain threshold that may be as low as 350 keV. Thus, in addition to a lower energy threshold, sophisticated scatter correction models have been developed to remove the residual scatter bias.³⁻⁵ The scatter background cannot be measured directly and must, instead, be estimated from the data. In a typical clinical imaging situation, the fraction of scattered events (SF) remaining even after applying an energy threshold can be as high as 40% or greater of the total events in the image.

The random coincidence rate (R) is proportional to the square of the radiation (singles rate) incident on the detectors. This radiation arises not only from the radioactivity in the field of view of the scanner, but also from radioactivity outside the field of view when one of the 2 photons from a given positron annihilation enters the scanner field-of-view and reaches the detectors. For whole-body clinical imaging with FDG, the radiopharmaceutical distributes throughout the body and radioactivity that localises in regions not within the field of view of the scanner increases the overall randoms rate to a level that may exceed 50% of the total acquisition rate. The randoms rate can be estimated from the singles rate (and the coincidence time window), or from a direct measurement of delayed events acquired in an out-of-time window. The advantage of a direct measurement of randoms is that it can account for any spatial variations in the distribution, while the disadvantage is that, as a measurement, it increases the noise.

Attenuation and Attenuation Correction

Annihilation photons that scatter are not only assigned to the incorrect line-of-response (LOR), as shown in Figure 2a, but they are also removed from the correct LOR. The removal of annihilation events from an LOR, either by

Compton scattering or photoelectric absorption, is termed attenuation. This is shown schematically in Figure 3a. Attenuation of 511 keV photons follows the usual exponential absorption determined by the linear attenuation coefficient $\mu(x, E)$, where x is the path length in tissue and E is the photon energy, that is, $E = 511$ keV for PET. An advantage of PET is that, for true coincidences, both annihilation photons must traverse the tissue without interaction and hence the attenuation for an LOR is dependent only on the total thickness of tissue. The ACF for a given LOR is obtained by integrating the linear attenuation coefficients along the path of the LOR (Fig. 3a). The limits of integration, x_1 and x_2 , are coordinates, measured along the LOR (k), at the entrance and exit of the patient. Since the correction does not depend on depth, the factors can be measured directly (Fig. 3b). The measurement is analogous to a CT scan acquired at 511 keV, rather than at 70 keV as it would be for clinical CT. Up to 3 ⁶⁸Ge rod sources (R) covering the full axial extent of the scanner circulate around the patient to acquire the corresponding transmission data at 511 keV.⁶ The total transmission counts, $I(k)$, acquired for a given LOR (k) is compared to the non-attenuated counts, $I_0(k)$, acquired in the absence of a patient (blank scan) and the ratio $I_0(k)/I(k)$ gives the ACF for LOR (k). By measuring this ratio for all LORs, the effect of attenuation can be corrected in the emission data.

For PET, the attenuation correction procedure is, in principle, exact. However, since the correction is based on a measurement involving photon counting statistics, additional noise is introduced into the PET data. The radioactivity in the rod sources is limited to avoid excessive dead time in the adjacent PET detectors, and transmission scan times may represent 40% or more of the total scan duration. Some of these issues have been addressed by simultaneous acquisition of the emission and transmission data⁷ via the use of different transmission sources, such as point sources of ¹³⁷Cs operated in singles mode⁸ and, more recently, the use of CT-based attenuation correction in combined PET/CT scanners,⁹ which is discussed in the section on “Imaging Technology for PET/CT”. The use of a cesium source reduces the noise in the transmission images by acquiring 50 to 100 times more singles counts than can be acquired in coincidence mode with ⁶⁸Ge rod sources.

For whole-body imaging of large patients, the ACFs can be significant, exceeding a factor of 100 for LORs through the shoulders and abdomen, thereby amplifying the intrinsic noise in the PET emission data. Despite the noise amplification, the importance of correcting for attenuation in whole-body FDG scans is illustrated in Figure 4, which shows the uncorrected image (Fig. 4a) and the corrected image (Fig. 4b). Artificially increased uptake in the skin

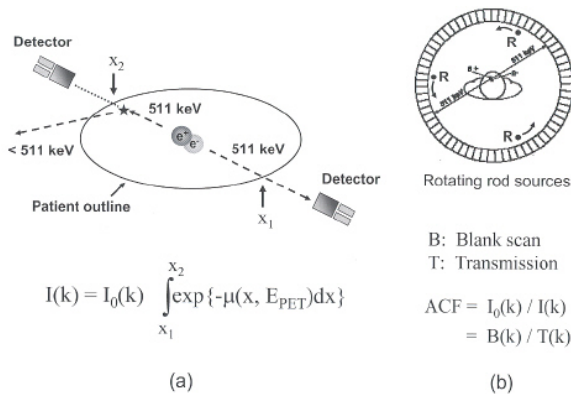


Fig. 3. The physics of PET attenuation and a procedure for correction of the attenuation effect: (a) An annihilation photon scatters in the patient and the event is removed from that line-of-response (k). The attenuated activity $I(k)$ is given by the unattenuated activity $I_0(k)$ multiplied by an attenuation factor computed as shown as the integral along LOR (k) within the patient. Note that the attenuation factor will be the same for all points in the patient between x_1 and x_2 . (b) Up to 3 rotating rod sources (R) of ^{68}Ge can be used to measure the attenuation correction factor (ACF) for LOR (k). The ratio $I_0(k)/I(k)$ is estimated from a blank scan $B(k)$ acquired without a patient and a transmission scan $T(k)$ acquired with the patient positioned in the scanner.

and lungs, as well as non-uniform recovery of uptake in the liver and spleen, are well-known features of uncorrected FDG-PET images. The uncorrected images are also not quantitative and, for interpretation purposes, estimates of a standardised uptake value (SUV) will be inaccurate.

Imaging Technology for PET

The past decade has witnessed significant advances in the imaging technology available for PET, the pace increasing recently with the introduction of new fast scintillators and the incorporation of combined anatomical and functional imaging in the same scanner. This section will briefly review some of these developments in PET imaging technology including the basic block detector design, scintillator performance, two-dimensional (2D) and 3D imaging and reconstruction algorithms.

PET Block Detectors

The block detector was first developed by Casey and Nutt in the mid 1980s.¹⁰ Previous efforts to improve PET spatial resolution through the use of smaller scintillation detectors each coupled to a photomultiplier tube, became a difficult and expensive solution. In addition, the demand to increase the axial coverage of PET scanners by incorporating multiple detector rings into the design created complex and inconvenient coupling schemes to extract the scintillation signals. Multiplexing first 32 and then 64 detectors to only 4 phototubes, Casey and Nutt¹⁰ decreased both complexity and cost in a single design. The basic principle of the block is shown in Figure 5. A block of scintillator is cut into 8×8 detectors and bonded to 4

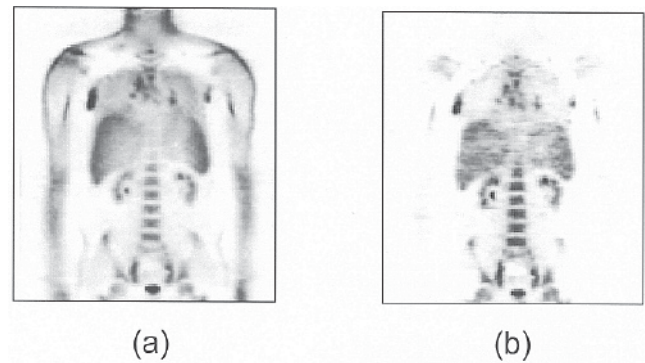


Fig. 4. A coronal section through a whole-body FDG-PET image of a patient; the images have been reconstructed (a) without correction for attenuation, and (b) with correction for attenuation, obtained as described in Figure 3. Note in the uncorrected image (a) the artifactual appearance of increased activity in the lungs, skin and periphery of the liver as compared to the corrected image (b).

photomultipliers. Light sharing between the 4 phototubes (A to D) is used to localise the detector in which the incident photon interacted. The principle is similar to that of the Anger logic used in a standard gamma camera, except that the scintillator block is physically cut into pixels. As shown in Figure 5, the depth of the cuts varies so as to minimise the overlap probability between adjacent detectors. The coordinates of the detector with the greatest probability of interaction are given by $X = [(D+B)-(C+A)]/\Sigma$ and $Y = [(A+B)-(C+D)]/\Sigma$, where $\Sigma = A+B+C+D$ is the total output from all 4 phototubes; Σ is proportional to the total energy deposited in the scintillator by the incident photon. Figure 5 also shows the distribution of signal peaks and valleys in a typical block illuminated with a uniform source of radioactivity, and a profile through the distribution showing good separation of the individual detectors. A block-specific lookup table determined during setup associates the X, Y co-ordinates with a particular detector element. The block design shown in Figure 5 has been the basic detector component in all multi-ring PET scanners for >15 years.

Scintillators for PET

The first PET scanners, developed in the early 1970s, were based on various geometrical configurations of thallium-activated sodium iodide crystals (NaI(Tl)), a scintillator that is widely used in standard nuclear medicine gamma cameras to detect the 140 keV photons from the decay of ^{99m}Tc . To detect 511-keV annihilation photons, however, the low density of sodium iodide is a disadvantage unless thicker crystals are used to compensate for the reduced stopping power. In the late 1970s, bismuth germanate (BGO), a denser scintillator with greater stopping power than sodium iodide, was first introduced as a prospective detector for PET.¹¹ Compared to NaI(Tl) , the

greater density and photofraction of BGO offer improved sensitivity by detecting a greater fraction of the incident photons. The light output of BGO is only about 15% of NaI(Tl) and the decay time is about 30% longer. Despite these suboptimal properties, BGO became established as the most widely-used scintillator for PET. Some of the physical properties of NaI(Tl) and BGO are compared in Table 1. Nevertheless, the use of NaI(Tl) for PET imaging continued and one company in particular, UGM Medical (Philadelphia, PA, USA), successfully developed PET scanners based on large NaI(Tl) crystals that were thicker than those used in conventional gamma cameras.¹²

From the late 1980s, the BGO block detector became a standard for PET imaging. Blocks of scintillator 50 mm x 50 mm in size and 20 mm to 30 mm deep were cut into 8 x 8 crystals and bonded to 4 one-inch photomultiplier tubes (Fig. 5). Two contiguous rings of blocks covered an axial extent of 10 cm with 16 rings of detectors each approximately 6 mm x 6 mm in size. The addition of a third ring of blocks covering a total of 15 cm axially with 24 rings of detectors appeared in PET scanners in the early 1990s and remained one of the most popular configurations for clinical PET scanning throughout the decade.¹³ The energy resolution and count rate performance of these multi-ring scanners were limited by the physical characteristics of BGO and a search for the ideal PET scintillator was initiated, a scintillator that would have greater light output and shorter decay time than BGO.

The introduction of new, faster scintillators such as gadolinium oxyorthosilicate (GSO)¹⁴ and lutetium oxyorthosilicate (LSO),¹⁵ both doped with cerium, has significantly improved the performance of PET scanners for clinical imaging. The physical properties of these newer scintillators are also compared in Table 1. Both GSO and LSO have much shorter decay times than BGO by a factor of 6 to 7, reducing system deadtime and improving the count rate performance, particularly at high activity levels in the field of view. Of even more importance for clinical imaging is the potential with faster scintillators to decrease the coincidence timing window, thereby reducing the

Table 1. Physical Properties of Different Scintillators for PET

Property	NaI	BGO	LSO	GSO
Density (g/mL)	3.67	7.13	7.4	6.7
Effective Z	51	74	66	61
Attenuation length (cm)	2.88	1.05	1.16	1.43
Decay time (ns)	230	300	35-45	30-60
Photons/MeV	38,000	8200	28,000	10,000
Light yield (%NaI)	100	15	75	25
Hygroscopic	Yes	No	No	No

BGO: bismuth germanate; GSO: gadolinium oxyorthosilicate; LSO: lutetium oxyorthosilicate; NaI: sodium iodide

randoms coincidence rate (see section on “Scatter and Randoms”). The increased light output of the new scintillators improves the energy resolution because the increased number of ultraviolet (UV) photons reduces the statistical uncertainty on the energy measurement. However, other physical effects contribute to the emission process and the improvement in energy resolution is not a simple function of the number of UV photons. The increased light output also improves the positioning accuracy of a block detector (Fig. 5), offering the possibility to cut the blocks even finer into smaller crystals to improve the spatial resolution. Unlike NaI(Tl), BGO, LSO and GSO are not hygroscopic, making packaging of the detectors easier. GSO is somewhat less rugged and more difficult to machine than either BGO or LSO, and LSO has an intrinsic radioactivity of about 280 Bq/mL with single-photon emissions in the range of 88 keV to 400 keV. Such a radioactive component is of little consequence for coincidence counting at 511 keV.

Imaging without Septa

PET is intrinsically a 3D imaging methodology, replacing the physical collimation required for single-photon imaging with the electronic collimation of coincidence detection. However, the first multi-ring scanners incorporated septa, lead or tungsten annular shields mounted between the detector rings (Fig. 6a). The purpose of the septa was to shield the detector rings from photons that scattered out of the transverse plane (Fig. 2a), thus restricting the use of electronic collimation to within the plane. This restriction also allows 2D reconstruction algorithms to be used on a plane-by-plane basis rather than requiring a full 3D reconstruction algorithm. However, by restricting annihilation events to a set of 2D planes, inefficient use is made of the emitted radiation (Fig. 6b). When the septa are extended (Fig. 6b, top), only LORs with small angles of incidence are active; the remainder intersect the septa and do not reach the detectors. When the septa are retracted (Fig. 6b, bottom), many more LORs are active and the overall scanner sensitivity increases by a factor of 6 or greater, depending on the design.¹⁶ The first multi-ring PET scanners with retractable septa that could acquire data in either 2D or 3D mode appeared in the early 1990s.¹⁷

Since the scatter and randoms rates also increase, any estimation of the net benefit of 3D imaging compared to 2D imaging must take into account these increases, and not just the increase in true coincidence events. The scatter fraction, for example, increases by a factor of at least 3 compared to 2D imaging and randoms rates increase by a similar or greater factor.¹⁶ A measure of actual improvement in signal-to-noise is the noise equivalent count rate (NECR),¹⁸ defined by the expression $T^2/(T + S + \alpha R)$ where T, S and R are the true, scattered and random coincidence rates, respectively.

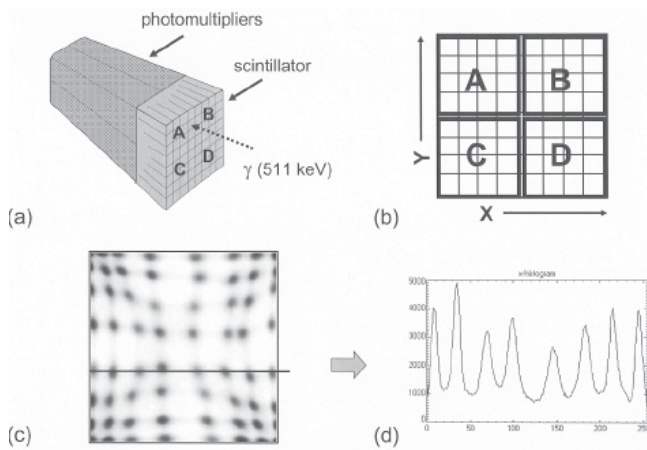


Fig. 5. The concept of the PET block detector design: (a) a block of scintillator is partitioned into 8×8 small elements with cuts of different depths. The scintillator is bonded to 4 photomultiplier tubes A to D. An incident 511 keV annihilation photon is converted to ultraviolet light and detected by the phototubes. (b) The sharing of the light between the 4 phototubes depends on the depth of the cuts and allows the detector element to be localised. (c) Uniform illumination of the detector with a 511 keV source demonstrates resolution of the individual elements even though they do not necessarily lie on a square grid due to the different gains of the phototubes. (d) A profile across the localisation map shows good separation of the peaks.

The improvement in signal due to the increase in true counts (from retracting the septa) is accompanied by an increase in statistical noise on T, the scattered events S and the randoms R, as expressed in the denominator of the NECR. The factor α is 2 for on-line randoms subtraction from the delayed coincidence window (see section on “Attenuation and Attenuation Correction”) and 1 for noiseless randoms subtraction. Smoothing the randoms before subtraction therefore corresponds to $1 < \alpha < 2$. The NECR is shown in Figure 6c as a function of activity concentration in a 20 cm diameter uniform cylinder for 2D and 3D acquisition mode. The significant improvement in the 3D NECR, and hence signal-to-noise, at lower activity concentrations is evident from the curves.

While the curves in Figure 6c highlight the benefits of 3D imaging for the brain, whole-body imaging in 3D has been more problematic. This is mainly because of the difficulty of shielding the detectors from activity outside the field-of-view when the septa are retracted. Recently, however, a number of factors have significantly improved the image quality that can be achieved for whole-body 3D imaging. These factors include advances in reconstruction algorithms, more accurate scatter correction, and the introduction of new, faster scintillators as described in the section on “Scintillators for PET”.

The progress in reconstruction has primarily been the introduction of statistically-based algorithms into the clinical

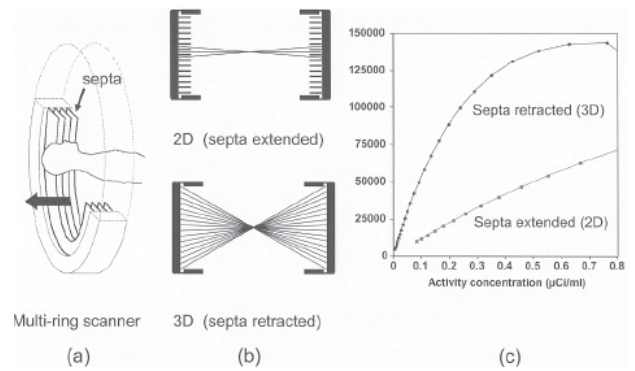


Fig. 6. (a) Schematic of a multi-ring PET scanner with inter-ring lead septa to shield the detector rings from out-of-plane scatter and randoms, (b) with the septa extended into the field-of-view the number of active lines-of-response is limited to those in-plane and small incident angles (top), whereas with the septa removed (bottom) the number of active lines-of-response is greatly increased, thereby increasing the sensitivity, (c) the Noise Equivalent Count Rate (NECR) as a function of activity concentration in the field-of-view showing the significantly improved performance in 3D mode with the septa retracted, particularly at the lower concentrations.

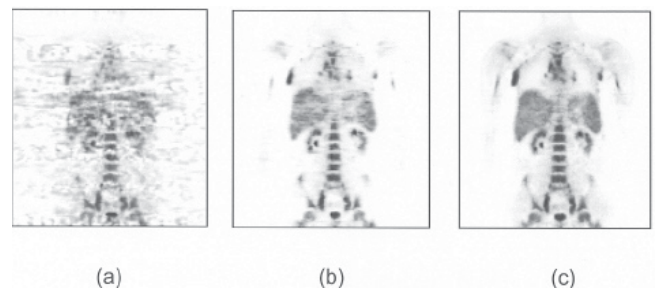


Fig. 7. An FDG-PET whole-body scan acquired in 3D mode with septa retracted and reconstructed using (a) 3D filtered back-projection algorithm with reprojection, (b) FORE plus OSEM, and (c) FORE plus AWOSEM.

setting. One of the earliest and most widely used 3D reconstruction algorithms is the reprojection approach based on a 3D extension of the original 2D, filtered backprojection algorithm.¹⁹ While this approach works well for the lower noise environment of brain imaging, the quality for whole-body imaging is less than optimal (Fig. 7a). The development of Fourier rebinning (FORE)²⁰ enabled 3D data sets to be accurately rebinned into 2D data sets and reconstructed in 2D with a statistically-based algorithm such as ordered-subset expectation-maximisation (OSEM).²¹ This is shown in Figure 7b for the same data set as Figure 7a. The improvement in image quality compared to Figure 7a is significant, although some non-uniformity remains in the liver and spleen. Further progress has been made by incorporating attenuation information into the reconstruction model in the form of weighting factors (Fig. 7c). The activity in the liver and spleen shows improved uniformity and the overall image quality is superior with

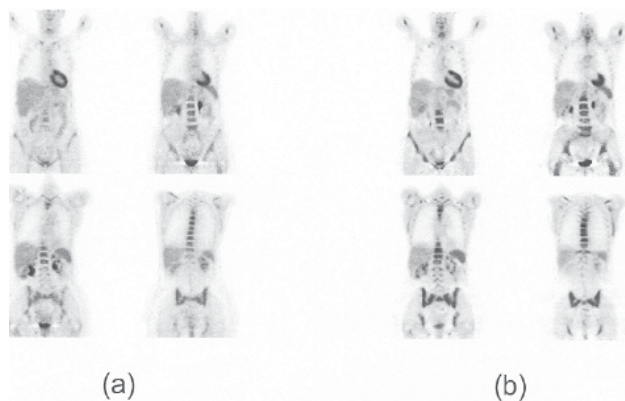


Fig. 8. A 72 kg female patient injected with 762 MBq of FDG and scanned first at 64 minutes in 2D mode with septa extended and then at 166 minutes in 3D mode with septa retracted. Both scans were acquired for 9 minutes emission and 3 minutes transmission: (a) 4 coronal sections from the 2D mode acquisition and (b) the same 4 coronal sections from the 3D mode acquisition. Owing to the time delay between the 2 scans, some of the differences will be physiological; the equivalent injected activity for the 3D scan is 400 MBq. (Data courtesy of Kettering Memorial Hospital, Kettering, Ohio).

the use of FORE and attenuation-weighted OSEM (AWOSEM).²² The FORE+AWOSEM approach is an example of a hybrid 3D algorithm, where the data are acquired in 3D, rebinned to 2D and reconstructed with a 2D algorithm. Other similar combinations are possible, such as the 2.5-dimensional row action maximum likelihood algorithm (RAMLA) developed by Daube-Witherspoon et al,²³ and used for clinical imaging. A second advance that has contributed to the improved image quality in 3D whole-body imaging has been progress in scatter correction algorithms. In particular, the development of faster, image-based algorithms²⁴ has improved accuracy. The elevated levels of scatter encountered in 3D imaging can be accurately estimated from the emission and transmission data and subtracted from the reconstructed images. Finally, one of the most significant factors contributing to the adoption of 3D acquisition for clinical whole-body imaging has been the introduction of new, faster scintillators (see section on “Scintillators for PET”). For LSO, in particular, a shorter coincidence time window, reduced dead time and improved energy resolution compared with a corresponding BGO scanner increases the maximum NECR, and improves the signal-to-noise.

To illustrate the comparison between 2D and 3D imaging, an example of a 72-kg patient imaged first in 2D mode with septa extended and then in 3D mode with septa retracted is shown in Figure 8. The 2D images (Fig. 8a) were acquired 1 hour after injection, and the 3D images (Fig. 8b) were acquired 3 hours after injection, when the activity level had decayed by an additional factor of 1.9. The data were

reconstructed with AWOSEM and for a patient of this size, the 2D and 3D image quality is quite comparable. Accounting for the extra decay factor, the 3D study could have been acquired with either half the injected activity or for half the scan time. Although qualitative and subjective, this is nevertheless an example of the considerable progress that has been made in 3D whole-body imaging.

Imaging Technology for PET/CT

The development of the combined PET/CT scanner²⁵⁻²⁷ represents an evolution in imaging technology. While superficially it may seem that, in most cases, it would be equally effective to view the CT and PET images from a given patient on adjacent screens, a consensus is emerging that accurately-aligned fused images of anatomy and function for every patient offer substantial advantages, adding greatly to the confidence with which a study is interpreted.²⁸⁻³¹ This section reviews the rationale for developing combined PET/CT technology, outlines an algorithm for CT-based attenuation correction and describes existing PET/CT designs and protocols for combined PET/CT imaging.

Rationale for PET/CT

Accurate anatomical localisation of functional abnormalities is a well-known difficulty for PET, even with a non-specific tracer such as FDG where some limited anatomical information is available from the uptake in muscles, brain and heart and excretion through the kidneys and bladder. In oncology particularly, while a positive PET reading may be the first step in diagnosing or staging disease, more detailed information such as precise localisation to a lymph node, or in bone or soft tissue can guide the appropriate treatment decision, or assess a response to therapy. Such localisation accuracy is difficult from the FDG-PET images alone, and the contrast in the low spatial resolution PET transmission scan is insufficient to visualise soft tissue structures, or even, in many cases, bone.

It is well known, of course, that CT and PET scans of the same patient acquired on different scanners can be aligned using one of a number of available software methods,³²⁻³⁴ even though the algorithms are often labour-intensive and, outside the brain, may fail to converge to a satisfactory solution. An alternative approach, therefore, is to combine the imaging technology of CT and PET into one scanner such that both anatomy and function, accurately aligned, are imaged in a single scan session. Some of the drawbacks of the software approach and the way in which they are addressed by the recently-developed hardware approach are summarised in Table 2. Of particular importance is the positioning of the patient, the use of the same bed for both scans and minimisation of the effect of uncontrollable internal organ movement. For non-specific tracers, such as

Table 2. Drawbacks of Software Fusion Resolved by the Hardware Approach

Software fusion	Hardware fusion
Access to image archives required	Images immediately available
Carefully-controlled patient positioning	Single-patient positioning
Different scanner bed profiles	Same bed for both scans
Internal organ movement	Little internal organ movement
Disease progression in time	Scans acquired close in time
Limited registration accuracy	Improved registration accuracy
Inconvenience for patient (2 scans)	Single, integrated scan
Labour intensive registration algorithms	No further alignment required

FDG with benign accumulation in tissue and organs, it is important, especially in the abdomen and pelvic region, to distinguish normal uptake from pathology. Since accurate localisation is routinely available with combined PET/CT scanning, such a distinction is straightforward in most cases.

While there are many technical reasons to prefer the hardware approach to image fusion (Table 2), as described above, the convenience to both patient and physician should not be underestimated. For the patient, 1 appointment and a single scan session is required to obtain complete anatomical and functional information related to his or her disease. For the physician, the potential to have accurately registered CT and PET images available at the same time and on the same viewing screen offers unique possibilities. The added confidence in reading the study comes from the accurate localisation of tracer accumulation, the distinction of normal uptake from pathology, and the verification that a suspicious finding on one modality can be confirmed by the other modality. In some cases, a suspicious finding on one modality invites a closer examination of the other modality; a retrospective image review that can take place immediately the PET/CT scan has concluded.

CT-based Attenuation Correction

The acquisition of accurately co-registered anatomical and functional images is a major strength of the combined PET/CT scanner. However, an additional advantage of the hardware fusion approach is the potential to use the CT images for attenuation correction of the PET emission data, eliminating the need for a separate, lengthy PET transmission scan (see section on “Attenuation and Attenuation Correction”). The use of the CT scan for attenuation correction not only reduces whole-body scan times by at least 40%, but also provides essentially noiseless ACFs compared to those from standard PET transmission

measurements. The attenuation values are energy dependent. Hence, the correction factors derived from a CT scan at a mean photon energy of 70 keV must be scaled to the PET energy of 511 keV.

Scaling algorithms typically use a bilinear function to transform the attenuation values above and below a given threshold with different factors. One algorithm⁹ sets the threshold at 300 HU because pixels >300 HU are assumed to have a bone-related content (spongiosa or cortical). Other algorithms³⁵ set the change in scale factor at 0 HU, assuming that pixels >0 HU can be represented by a mixture of water and bone, while pixels <0 HU are represented by a mixture of water and air. However, some tissue types, such as muscle (~60 HU) and blood (~40 HU), are >0 HU and yet are clearly not a water-bone mix. Indeed, since there is no unique transformation, different approaches may be equally valid and lead to only small differences in the transformed coefficients. The scaled CT images are interpolated from CT to PET spatial resolution and the ACFs are then generated by reprojection of the interpolated images.

Iodinated contrast is used in CT to enhance attenuation values in the vasculature (intravenous administration) and gastrointestinal tract (oral administration). Contrast-enhanced pixels that are incorrectly scaled to 511 keV can potentially generate focal artifacts in the PET image. This would be an undesirable outcome, particularly for tumour imaging. Of course, avoiding the administration of contrast would eliminate the problem. However, standard-of-care CT scanning generally dictates the use of either intravenous or oral contrast, or both as in the case of the abdominal and pelvic regions. One obvious way to avoid such problems is to perform 2 CT scans: a clinical CT with appropriate contrast administration, and a low-dose, non-contrast CT for attenuation correction and co-registration. This 2-scan approach, however, would further increase the radiation exposure to the patient. Recent results³⁶ have shown that the presence of intravenous contrast at normal concentrations actually has little effect on the CT-based ACFs. Unfortunately, this is not the case for oral contrast where the larger intestinal volumes and wide range of concentrations can lead to over-correction of the PET data. However, Carney et al³⁷ have shown that a modification can be made to the original algorithm of Kinahan et al⁹ to separate contrast-enhanced CT pixels from those of bone. Since the presence of iodinated contrast has a negligible effect (<2%) on photon attenuation at 511 keV, the CT image pixels identified as oral contrast can be set to a tissue-equivalent value thus ensuring accurate ACFs for the PET data. This modified algorithm can, to a considerable extent, also reduce artifacts due to catheters and metallic objects in the patient.³⁸

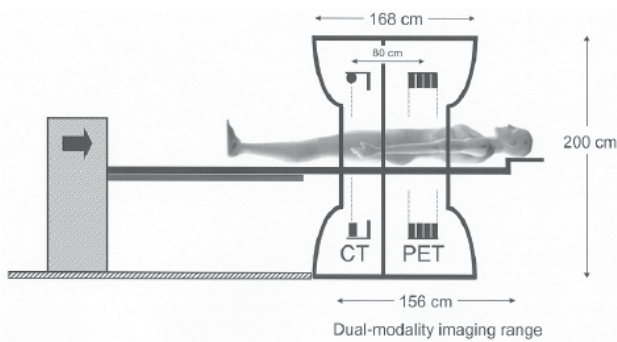


Fig. 9. A schematic of a current PET/CT scanner design currently marketed by Siemens as the *biograph* (Siemens Medical Solutions, Chicago, IL) and by CTI Molecular Imaging as the *Reveal* (CTI Molecular Imaging, Knoxville, TN). The design incorporates a multi-detector spiral CT scanner and an LSO PET scanner. The dimensions of the gantry are 228 cm wide, 200 cm high and 168 cm deep. The separation of the CT and PET imaging fields is about 80 cm. The co-scan range for acquiring both CT and PET is 156 cm (182 cm, feet first). The patient port diameter is 70 cm.

Current Technology for PET/CT

Since the development and clinical evaluation of the first prototype PET/CT scanner,²⁵⁻³¹ the commercial realisation of the concept has already undergone a number of refinements. One such design, manufactured by CPS Innovations (Knoxville, TN, USA) is shown schematically in Figure 9. The design comprises a 2 or 16-slice Siemens spiral CT (Siemens Medical Solutions, Forchheim, Germany) with an LSO-based ECAT Accel without septa that is operated entirely in 3D acquisition mode (CPS Innovations, Knoxville, TN, USA). Also, since no PET transmission sources are incorporated into the design, CT-based attenuation correction (See section on “CT-based Attenuation Correction”) is standard on these systems. Of note in this, and other commercial designs, is the minimal level of actual hardware integration. Both scanners are placed in tandem within the gantry housing. The gantry is

200-cm high and 228-cm in width. The overall length is 168 cm with an axial separation of the centre of the CT and PET fields-of-view of about 80 cm. The patient handling system or couch eliminates vertical deflection of the pallet as it moves through the tunnel. Instead of the usual design where the pallet moves over a fixed support such that the cantilever point changes, in this design the pallet is attached to a pedestal at a fixed point and the entire assembly moves into the scanner as a single unit on floor-mounted rails. The co-scan range for combined CT and PET imaging is 156 cm and the patient port diameter is 70 cm.

This design is marketed by Siemens Medical Solutions as the *biograph* and by CTI Molecular Imaging as the *Reveal*. Other vendors, notably General Electric and Philips Medical offer their own versions of the combined PET/CT scanner. The design from General Electric is the *Discovery* series and that from Philips is the *Gemini*. While the General Electric design is similar to that of CPS Innovations, the Philips approach is more open with the CT and PET kept separate to allow access between the scanners. Some characteristic features of the CT and PET components of the different designs are summarised in Tables 3 and 4, respectively.

PET/CT Clinical Protocols

Following the clinical evaluation of the prototype PET/CT scanner²⁸⁻³¹ from 1998 to 2001, there has been less than 3 years’ experience with combined PET/CT imaging on commercial scanners in the clinical arena. Imaging protocols, particularly for oncology, are therefore still being defined and evaluated,³⁹⁻⁴⁴ and it will doubtless be a while before they become as well-established as they are for CT. Issues of respiration, contrast, CT operating parameters, PET scan time, optimal injected dose of FDG and others must be carefully addressed before definitive PET/CT protocols for specific clinical applications emerge. Nevertheless, there will be certain common features to the

Table 3. Characteristics of Current PET/CT Designs: CT Components

Specification	Reveal RT <i>biograph</i> duo	Reveal XVI <i>biograph</i> 16	Discovery		Gemini
			LS	ST	
Detector type	UFC	UFC	Ceramic	Ceramic	Cadmium tungstate
CT detector rows	2	16	4, 8	4, 8, 16	2
Rotation speed (s)	0.8	0.42	0.5	0.5	0.5
Anode heat (MHU)	3.5	5.3	6.3	6.3	6.5
Transaxial FOV (cm)	50	50	50	50	50
Max spiral scan (sec)	100	100	120	120	100
Min slice width (mm)	1	0.75	0.625	0.625	0.5
CT patient port (cm)	70	70	70	70	70
Reconstruction (s)	1.0	0.17	0.5	0.5	0.5

CT: computed tomography; FOV: field-of-view; MHU: Mega Heat Unit; UFC: ultrafast ceramic. The reconstruction time is the time to reconstruct a single CT slice.

Table 4. Characteristics of Current PET/CT Designs: PET Components

Specification	Reveal	Discovery		Gemini
	<i>biograph</i>	LS	ST	
Scintillator	LSO	BGO	BGO	GSO
Detector size (mm ²)	6.4 x 6.4	4.0 x 8.0	6.2 x 6.2	4.0 x 6.0
Detector depth (mm)	25	30	30	20
Axial FOV (cm)	16.2	15.2	15.2	18.0
Septa	3D only	2D/3D	2D/3D	3D only
Attenuation correction	CT	CT and ⁶⁸ Ge rods		CT and ¹³⁷ Cs
Transaxial FOV (cm)	58.5	55	60	57.6
Co-scan range (cm)	156/182	160	160	195
Spatial resolution (3D; mm)	6.3	4.8	6.2	4.8
PET patient port (cm)	70	59	70	63

BGO: bismuth germanate; CT: computed tomography; FOV: field-of-view; GSO: gadolinium oxyorthosilicate; LSO: lutetium oxyorthosilicate; NaI: sodium iodide; PET: positron emission tomography

The co-scan range is the maximum axial extent that can be covered by both CT and PET. The transmission sources offered with the Discovery and the Gemini are optional. Spatial resolution is measured at 1 cm off axis. For the Discovery LS and the Gemini, the PET patient port diameter is <70 cm.

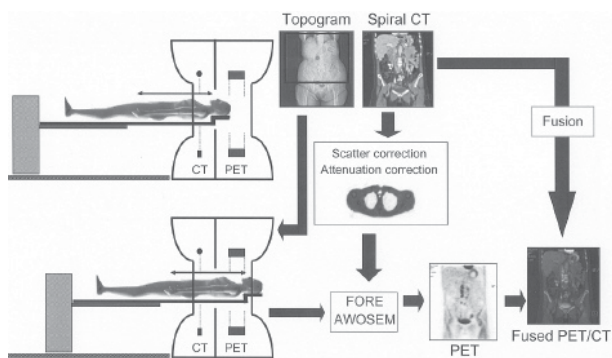


Fig. 10. A typical imaging protocol for a combined PET/CT study that includes: a topogram, or scout, scan for positioning, a spiral CT scan, generation of CT-based ACFs, a PET scan over the same axial range as the CT scan, reconstruction of the attenuation-corrected PET emission data and display of the final fused images.

protocols; these are outlined schematically in Figure 10 for a typical PET/CT scan.

As for any FDG-PET scan, following an injection of 10 mCi to 15 mCi of FDG and a 1-hour uptake period, the patient is positioned in the scanner. For PET/CT, the first step (Fig. 10) is a topogram, or scout scan, acquired over a range of 50 cm to 100 cm. The total range to be scanned by both PET and CT is then defined on the topogram, based on the particular indication for the study (that is, skull base to abdomen for head and neck malignancies, and neck through upper thigh for most other malignancies; for melanoma, the scan range covers head to toe, if possible). An appropriate respiration protocol must be defined and implemented to minimise the mismatch between CT and PET. In the absence of respiratory gating, a good match is found if the CT is acquired with partial or full expiration, and the PET with shallow breathing. This is feasible with the 16-slice CT scanner where a scan of the thorax and abdomen can

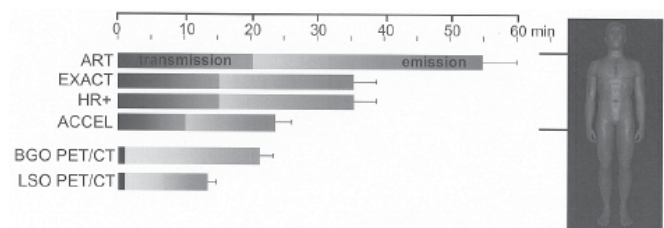


Fig. 11. A graph that shows the reduction in whole-body PET scan duration for different generations of scanners, from the rotating ART scanner at almost an hour to the multi-ring BGO scanners that required 35 minutes total with 10 minutes for the transmission scan. Scan times for LSO scanners are typically around 25 minutes. For the PET/CT scanners, scan times close to 10 minutes can be achieved by eliminating the transmission scan and using CT-based attenuation correction.

take as little as 15 s. Upon completion of the spiral CT scan, the patient couch is advanced into the PET field-of-view and a multi-bed PET scan acquired over the same range as the CT. The reconstruction of the CT images occurs in parallel with the acquisition of the PET data, allowing the calculation of the scatter and ACFs to be performed during the PET acquisition. The CT-based ACFs are calculated according to the algorithm of Kinahan et al,⁹ and once the acquisition for the first bed position is completed, PET reconstruction can commence. The 3D reconstruction is performed using FORE and AWOSEM.²² Within a few minutes of the conclusion of the final PET bed position, attenuation-corrected and reconstructed PET images are available for viewing, automatically co-registered with the CT scan by simply accounting for the axial shift between the CT and PET imaging fields-of-view.

The recent reduction in PET scan duration due to the new scintillator technology has been taken further by the introduction of the PET/CT scanner. The use of CT-based

ACFs eliminates the transmission scan (Fig. 11). Typical protocols are illustrated schematically for different scanners showing a reduction from 55 minutes a few years ago on the ECAT ART to a scan time of 25 minutes currently on the ECAT Accel, the LSO PET scanner. For all these protocols, the standard PET transmission scan with rotating rod or point sources represents about 40% of the total scan duration. However, for the PET/CT with CT-based attenuation correction, a whole-body spiral CT scan is acquired in 15 to 60 s, resulting in a total time for an LSO PET/CT scan of <15 min. For smaller patients of around 70 kg, even shorter scan times of <10 min result in images of good diagnostic quality.⁴⁵

The impact of this reduction in scan time will be very significant for an active clinical programme. The potential increase in patient throughput will create logistical problems when attempting to ensure a constant supply of patients, such as access to sufficient uptake rooms, increased shielding of the uptake area and radiation dose to the technologists. Above all, the shorter PET/CT scan times are more comfortable and tolerable for patients. Scans of the thorax and abdomen can also be acquired with the arms raised, thereby reducing or eliminating truncated images that often arise when the scan is acquired with the arms down.

Conclusions

Even though combined PET/CT scanners have been in production for less than 3 years, the technology is undergoing rapid evolution. For PET, the introduction of new scintillator materials, detector concepts and electronics is resulting in performance improvements in count rate, spatial resolution and signal-to-noise. At the same time, the increasing number of detector rows and reduction in rotation time are transforming whole-body CT performance. The combination of high performance CT with high performance PET is a powerful imaging platform for the diagnosis, staging and therapy monitoring of malignant disease. While the PET scanners incorporated into current PET/CT designs are still offered by some vendors for PET only applications, a high percentage of sales are now PET/CT with the prediction that PET scanners could be replaced entirely by PET/CT in the future. It is likely that there will then be a demand for a design that offers less performance at less cost. To meet this demand, an entry level or mid-range PET/CT is required, possibly in a form similar to the original prototype of PET detectors mounted on the same rotating assembly as the CT.²⁹ Since the performance of the PET components is the limitation on the overall imaging time, institutions requiring high throughput and large patient volumes will always demand the highest PET performance. Nevertheless, a 4- or 8-slice CT scanner may be adequate for most oncology applications, with a 16-slice

CT more appropriate for PET/CT applications in cardiology. As the current PET/CT technology becomes more widespread, appropriate future designs of this concept will doubtless emerge.

Acknowledgements

The author thanks Dr Ron Nutt, President of CTI Molecular Imaging, for his friendship, insight, leadership and contributions to the development of PET instrumentation for over 2 decades; Dr Thomas Beyer, University of Essen, for helping to pioneer the development of PET/CT; and Dr David Brasse, Institut de Recherches Subatomique, Strasbourg, France for the reconstructions presented in Figures 4 and 8. The author acknowledges the assistance of many friends and colleagues at CPS Innovations and the University of Pittsburgh PET Facility, and particularly Drs Jeffrey Yap, Jonathan Carney and Nathan Hall in the Departments of Medicine and Radiology, University of Tennessee, for many helpful discussions and continuing contributions. The PET/CT development project is supported by National Cancer Institute grant CA 65856.

REFERENCES

1. Weber WA, Avril N, Schwaiger M. Relevance of positron emission tomography (PET) in oncology. *Strahlenther Onkol* 1999;175:356-73.
2. Warburg O. On the origin of cancer cells. *Science* 1956;123:306-14.
3. Bailey DL, Meikle SR. A convolution-subtraction scatter-correction method for 3D PET. *Phys Med Biol* 1994;39:411-24.
4. Watson CC, Newport D, Casey ME. A single scatter simulation technique for scatter correction in 3D PET. In: Grangeat P, Amans J-L, editors. *Three-dimensional Image Reconstruction in Radiology and Nuclear Medicine*. Dordrecht: Kluwer Academic, 1996:255-68.
5. Ollinger JM. Model-based scatter correction for fully 3D PET. *Phys Med Biol* 1996;41:153-76.
6. Carroll LR, Kretz P, Orcutt G. The orbiting rod source: improving performance in PET transmission correction scans. In: Esser PD, editor. *Emission Computed Tomography: Current Trends*. New York: Society of Nuclear Medicine, 1983:235-47.
7. Meikle SR, Bailey DL, Hooper PK, Eberl S, Hutton BF, Jones WF, et al. Simultaneous emission and transmission measurements for attenuation correction in whole-body PET. *J Nucl Med* 1995;36:1680-8.
8. deKemp RA, Nahmias C. Attenuation correction in PET using single photon transmission measurement. *Med Phys* 1994;21:771-8.
9. Kinahan PE, Townsend DW, Beyer T, Sashin D. Attenuation correction for a combined 3D PET/CT scanner. *Med Phys* 1998;25:2046-53.
10. Casey ME, Nutt R. A multicrystal, two-dimensional BGO detector system for positron emission tomography. *IEEE Trans Nucl Sci* 1986;33:460-3.
11. Cho ZH, Farukhi MR. Bismuth germanate as a potential scintillation detector in positron cameras. *J Nucl Med* 1977;18:840-4.
12. Karp JS, Muehlelehner G, Geagan MJ, Freifelder R. Whole-body PET scanner using curved-plate NaI(Tl) detectors. *J Nucl Med* 1998;39:50P.
13. Wienhard K, Eriksson L, Grootenck S, Casey M, Pietrzyk U, Heiss WD. Performance evaluation of the positron scanner ECAT EXACT. *J Comput Assist Tomogr* 1992;16:804-13.

14. Takagi K, Fukazawa T. Cerium-activated Gd_2SiO_5 single crystal scintillator. *App Phys Lett* 1983;42:43-5.
15. Melcher CL, Schweitzer JS. Cerium-doped lutetium oxyorthosilicate: a fast, efficient new scintillator. *IEEE Trans Nucl Sci* 1992;39:502-5.
16. Townsend DW, Isoardi RA, Bendriem B. Volume imaging tomographs. In: Bendriem B, Townsend DW, editors. *The Theory and Practice of 3D PET*. Dordrecht: Kluwer Academic, 1998:111-32.
17. Spinks TJ, Jones T, Bailey DL, Townsend DW, Grootoonk S, Bloomfield PM. Physical performance of a positron tomograph for brain imaging with retractable septa. *Phys Med Biol* 1992;37:1637-55.
18. Strother SC, Casey ME, Hoffman EJ. Measuring PET scanner sensitivity – relating count rates in the image to signal-to-noise ratios using noise equivalent counts. *IEEE Trans Nucl Sci* 1990;37:783-8.
19. Kinahan PE, Rogers JG. Analytic three-dimensional image reconstruction using all detected events. *IEEE Trans Nucl Sci* 1990;36:964-8.
20. Defrise M, Kinahan PE, Townsend DW, Michel C, Sibomana M, Newport DF. Exact and approximate rebinning algorithms for 3D PET data. *IEEE Trans Med Imaging* 1997;16:145-58.
21. Hudson H, Larkin R. Accelerated image reconstruction using ordered subsets of projection data. *IEEE Trans Med Imaging* 1994;13:601-9.
22. Comtat C, Kinahan PE, Defrise M, Michel C, Townsend DW. Fast reconstruction of 3D PET data with accurate statistical modeling. *IEEE Trans Nucl Sci* 1998;45:1083-9.
23. Daube-Witherspoon ME, Matej S, Karp JS, Lewitt RM. Application of the row action maximum likelihood algorithm with spherical basis functions to clinical PET imaging. *IEEE Trans Nucl Sci* 2001;48:24-30.
24. Watson CC. New, faster, image-based scatter correction for 3D PET. *IEEE Trans Nucl Sci* 2000;47:1587-94.
25. Beyer T, Townsend DW, Brun T, Kinahan PE, Charron M, Roddy R, et al. A combined PET/CT scanner for clinical oncology. *J Nucl Med* 2000;41:1369-79.
26. Townsend DW. A combined PET/CT scanner: the choices. *J Nucl Med* 2001;3:533-4.
27. Townsend DW, Cherry SR. Combining anatomy with function: the path to true image fusion. *Eur Radiol* 2001;11:1968-74.
28. Charron M, Beyer T, Bohnen NN, Kinahan PE, Dachille M, Jerin J, et al. Image analysis in patients with cancer studied with a combined PET and CT scanner. *Clin Nucl Med* 2000;25:905-10.
29. Meltzer CC, Martinelli MA, Beyer T, Kinahan PE, Charron M, McCook B, et al. Whole-body FDG PET imaging in the abdomen: value of combined PET/CT. *J Nucl Med* 2001;42:35P.
30. Meltzer CC, Snyderman CH, Fukui MB, Bascom DA, Chander S, Johnson JT, et al. Combined FDG PET/CT imaging in head and neck cancer: impact on patient management. *J Nucl Med* 2001;42:36P.
31. Kluetz PG, Meltzer CC, Villemagne VL, Kinahan PE, Chander S, Martinelli MA, et al. Combined PET/CT imaging in oncology: impact on patient management. *Clin Positron Imaging* 2000;3:223-30.
32. Pelizzari CA, Chen GT, Spelbring DR, Weichselbaum RR, Chen CT. Accurate three-dimensional registration of CT, PET, and/or MR images of the brain. *J Comput Assist Tomogr* 1989;13:20-6.
33. Pietrzyk U, Herholz K, Heiss WD. Three-dimensional alignment of functional and morphological tomographs. *J Comput Assist Tomogr* 1990;14:51-9.
34. Woods RP, Mazziotta JC, Cherry SR. MRI-PET registration with automated algorithm. *J Comput Assist Tomogr* 1993;17:536-46.
35. Burger C, Goerres G, Schoenes S, Buck A, Lonn AH, von Schulthess GK. PET attenuation coefficients from CT images: experimental evaluation of the transformation of CT into PET 511-keV attenuation coefficients. *Eur J Nucl Med Mol Imaging* 2002;29:922-7.
36. Yau YY, Coel M, Chan WS, Tam YM, Wong S. Application of IV contrast in PET-CT: does it really produce attenuation correction error. *J Nucl Med* 2003;44:272P.
37. Carney JP, Beyer T, Brasse D, Yap JT, Townsend DW. Clinical PET/CT scanning using oral CT contrast agents. *J Nucl Med* 2002;45:57P.
38. Cohade C, Osman M, Marshall L, Wahl RL. Metallic object artifacts on PET-CT: clinical and phantom studies. *J Nucl Med* 2002;43:308P.
39. Keidar Z, Bar-Shalom R, Guralnik L, Yefremov N, Kagana O, Gaitini D, et al. Hybrid imaging using PET/CT with ^{18}F -FDG in suspected recurrence of lung cancer: diagnostic value and impact on patient management. *J Nucl Med* 2002;43:32P.
40. Dizendorf E, Ciernik IF, Baumert B, von Schulthess GK, Luetolf UM, Steinert HC. Impact of integrated PET/CT scanning on external beam radiation treatment planning. *J Nucl Med* 2002;43:33P.
41. Freudenberg LS, Antoch G, Mueller SP, Stattaus J, Eberhardt W, Debatin J, et al. Preliminary results of whole-body FDG-PET/CT in lymphoma. *J Nucl Med* 2002;43:30P.
42. Osman MM, Cohade C, Leal J, Wahl RL. Direct comparison of FDG-PET and PET-CT imaging in staging and re-staging patients with lung cancer. *J Nucl Med* 2002;43:151P.
43. Steinert HC, Hany TF, Kamel E, Lardinois D, Weder W, von Schulthess GK. Impact of integrated PET/CT scanning on preoperative staging of lung cancer. *J Nucl Med* 2002;43:151P.
44. Yeung HW, Schoder H, Larson SM. Utility of PET/CT for assessing equivocal PET lesions in oncology – initial experience. *J Nucl Med* 2002;43:32P.
45. Halpern B, Dahlbom M, Vranjesevic D, Ratib O, Schiepers C, Silverman DH, et al. LSO-PET/CT whole-body imaging in 7 minutes: is it feasible? *J Nucl Med* 2003;44:380P.